Preprint Title	Focused Ion Beam Induced Platinum Deposition with a Low Temperature Cesium Ion Source
Authors	Thomas H. Loeber, Bert Laegel, Feray Bakan Misirlioglu, Meltem Sezen, Edgar J. D. Vredenbregt and Yang Li
Publication Date	28 Feb. 2025
Article Type	Full Research Paper
ORCID® iDs	Thomas H. Loeber - https://orcid.org/0000-0003-4697-1761

Focused Ion Beam Induced Platinum Deposition with a Low Temperature Cesium Ion Source

T. H. Loeber*, B. Laegel[1], M. Sezen, F. Bakan Misirlioglu[2], E. J. D. Vredenbregt and Y. Li[3]

Address: [1]Nano Structuring Center (NSC), Rheinland-Pfälzische Technische Universität Kaiserslautern-Landau (RPTU), P.O. Box 3049, D-67653, Kaiserslautern, Germany; [2]Sabanci University Nanotechnology Research and Application Center (SUNUM), 34956, Istanbul, Turkey and [3]Department of Applied Physics, Eindhoven University of Technology, P.O. Box 513, 5600 MB Eindhoven, The Netherlands

Email: T. H. Loeber - loeber@physik.uni-kl.de

* Corresponding author

Abstract

In addition to precise milling, the deposition of material at a specific location on a sample surface is a frequently used process of Focused Ion Beam (FIB) systems. Here we report on the deposition of platinum with a new kind of cesium FIB in which the cesium ions are produced by a low-temperature ion source. The platinum was deposited at different acceleration voltages and ion beam currents. The deposition rate, the material composition and specific resistance were examined and compared with layers deposited at comparable settings with a standard gallium FIB. The deposition rate is found to be linearly dependent on current density. The rate is comparable for Cs^+ and Ga^+ under similar conditions, but the deposit has lower Pt content for Cs^+. The specific resistance of the deposit is found to be higher for Cs^+ than for Ga^+, and decreasing with increasing acceleration voltage.

Keywords

focused ion beam (FIB); FIB induced deposition (FIBID); cesium ion source; cold atom ion source

Introduction

The deposition of material at a certain spot on a sample surface is a powerful and useful feature of Focused Ion Beam (FIB) systems. At first, the deposition was used for circuit editing and as a protection layer before milling. Nowadays, the process is more far-reaching and 3D, magnetic or superconductive structures can be created [1] [2] [3] [4]. Also, specific mechanical structures on Atomic force (AFM) cantilevers can be made [5] [6]. In the literature, four theories are used to explain the complex process of focused ion beam induced deposition (FIBID) [5][7]: primary ion beam, thermal heat spike, excited surface atoms or secondary electrons (SE). So far, the SE theory is the most popular one, but none of them provide a definitive description because the FIBID is extremely complex and depending on a variety of parameters. Besides beam parameters such as acceleration voltage, beam current, ion dose, and dwell time, the precursor material and substrate have an influence on the effective deposition rate. Gallium (Ga) and helium (He) are the most often utilized ion species for FIBID [1][2][5]. Besides these standard FIB systems, new kinds of laser cooled ion sources have been developed in the last few years. One strength of these ion sources based on laser-cooled atoms is that many elements unavailable with conventional sources can be used. At least 27 elements, including both metals and non-metals, have successfully been laser-cooled [8]. Among these elements, rubidium (Rb) and cesium (Cs) are more advanced with respect to source development due to their relatively low requirements for the cooling laser. Milling [9] and as well as induced deposition of platinum (Pt) [10] and tungsten (W) [11] properties have been measured for a prototype FIB with an ultracold Rb^+source.

Further, Cs^+ laser cooled ion source (LoTIS) has been developed and characterized [12] [13]. Like the Rb^+ source, the Cs^+ LoTIS has also been incorporated in a ThermoFisher FIB column. ZeroK NanoTech Corporation has created commercially available Cs^+ FIB systems based on the aforementioned construction [14]. Loeber et al. have shown several advantages of the cold Cs^+ FIB in imaging [15] and milling [16] applications over standard Ga^+ FIBs. Compared to a standard Ga^+ FIB, the Cs^+ FIB can produce images with higher resolution and a larger depth of focus. Furthermore, the material contrast is greater in Cs^+ acquired images than in Ga^+ ones. For milling appli-

cations, Cs^+ can deliver more evenly etched pattern bottoms than Ga^+. With these benefits in applications established, microscopy and induced deposition studies help to investigate more properties of the Cs^+ FIB. With similar sources and FIB column design of the Cs^+ and Rb^+ FIB, it is useful to compare application works by these FIBs to understand the relative merits of ion sources based on alkali metals. Also, Cs^+ is a preferred ion species over Ga^+ for secondary ion mass spectroscopy (SIMS) applications because Cs^+ can induce higher secondary ion yields for several elements e.g. carbon, oxygen, hydrogen, etc. [17] [18] [19] which provides higher signal to noise for SIMS analysis. A disadvantage of using Cs^+ is a possible surface modification [20] [21] [22]. One aspect of this paper is to show whether it is at all possible to deposit Pt with Cs^+ ions or whether the surface modifications are dominating.

This work presents FIBID experiments using a Cs^+ FIB in comparison to results of layer deposition induced by Rb^+ and Ga^+. The Pt was deposited at different acceleration voltages and ion beam currents to evaluate the deposition rate and the specific resistance of the layer. To measure the grain structure and the material composition with energy-dispersive X-ray spectroscopy (EDS) lamellas for transmission electron microscopy (TEM) were prepared.

Experimental

Both the Cs^+ and the Rb^+ FIB are equipped with a standard Pt gas injection system (GIS). The Ga^+ FIB is a ThermoFisher Helios NanoLab 650 and uses a Multi GIS. The same precursor (trimethylplatinum) was used for all FIBID-Pt experiments. The precursor was heated to 40° C to create a gas flow through the GIS nozzle, with the exit of the nozzle kept about 100 μm above the sample surface. The chamber pressure of the Cs^+ and the Ga^+ FIB was about 5×10^{-7} mbar before deposition and 8×10^{-6} mbar during deposition. For growth rate characterization, Pt layers 20 µm by 1 µm were deposited on silicon (Si). The ion beam currents were changed while the pattern size was kept constant. With the Cs^+ FIB, ion current densities between 0.9 and 14.2 pA/μm^2 at acceleration voltages of 2, 5, 8, and 16 kV, respectively, were used. With the Ga^+ FIB patterns were deposited at current densities between 0.7 and 19.8 pA/μm^2 with acceleration voltage of 5, 8,

16 and 30 kV, respectively. The deposition time was varied with the ion beam current to achieve a layer thickness of approximately 1000 nm. The actual thickness of each layer was measured with a standard cross section using the Ga^+ FIB. All scanning electron microscope (SEM) images were taken with the NanoLab 650 dual beam system.

The resistivity of Ga^+ and Cs^+ FIBID-Pt was measured via the Cr-on-glass standards mentioned in Ref. [10] using the sample design displayed in Fig. 7(a). The pattern size was 35 µm by 1.5 µm. With the Ga^+ FIB current densities between 0.9 and 8.4 pA/μm^2 and acceleration voltage of 8, 16 and 30 kV, respectively, were used, while with the Cs^+ FIB current densities between 0.4 and 8 pA/μm^2 and acceleration voltage of 2, 5, 8 and 16 kV were utilized. To calculate their resistivity the NanoLab 650 dual beam system was used to determine the length and the cross section of each deposited layer.

The TEM lamella were prepared with a JEOL JIB 4601F FIB-SEM MultiBeam system. The sample characterization in terms of elemental composition and structure was done with a JEOL ARM 200F (S)TEM system equipped with an Oxford EDS Detector.

Results and Discussion

Deposit surface

First, to reveal possible surface modifications, Pt layers were deposited with Cs^+ ions at 16, 8, 5 and 2 kV, respectively, with a current density of 6 pA/μm^2 . For this, a small part of the Si substrate was gently milled with the Cs^+ FIB at 16 kV before the deposition, such that the native oxide and other contamination were completely removed at this location. With that, the influence of oxygen molecules on the deposited layer can be excluded. The layers, which have a dimension of 40 µm by 1 µm, were deposited across the boundary between the bare Si and the Si with its native oxide. A visual inspection with the SEM reveals surface bubbles on layers deposited at 2 and 5 kV (as shown in Fig. 1(a)). No significant differences can be seen in the size or density of the bubbles between deposition on Si (upper part) and Si with the native oxide layer (lower part). Similar to Rb^+ FIBID-Pt discussed in Ref. [10], these bubbles appear after exposure to air of the samples (during

the short transfer from Cs^+ FIB to Ga^+ FIB) and are more numerous and larger at 2 kV compared to 5 kV. At higher acceleration voltages no bubbles can be observed (see Fig. 1(b) and (c)).

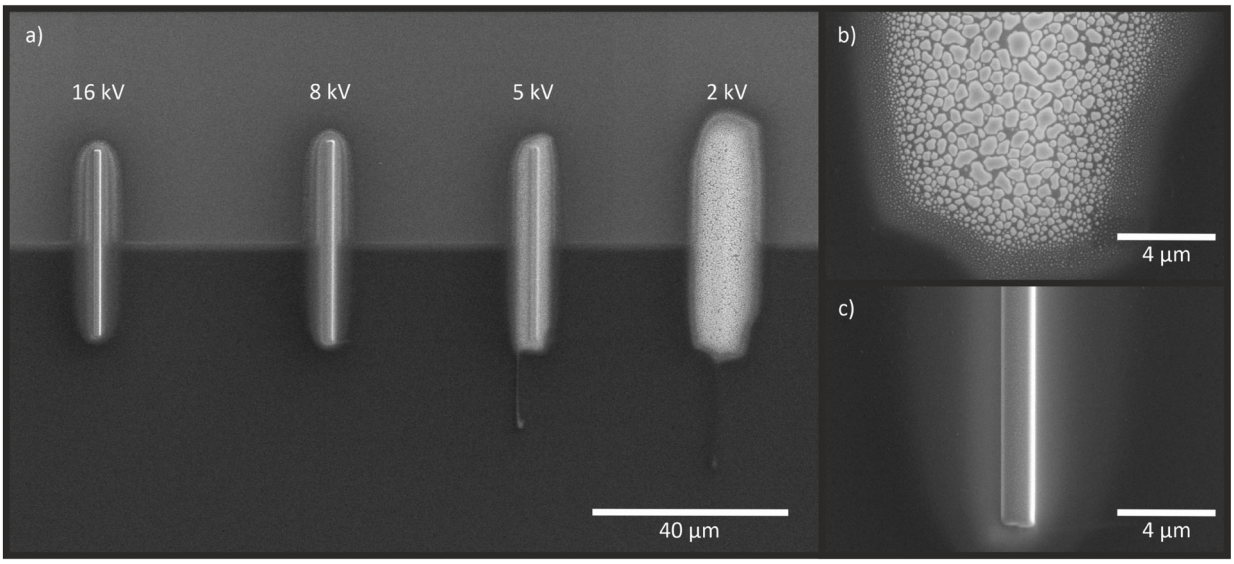

Figure 1: (a) SEM images of Pt deposited with Cs^+ ions at 16, 8, 5, and 2 kV on Si. The upper part of the image appears brighter because the native oxide of Si was removed before the deposition. The amount of surface bubbles increases with decreasing acceleration voltage, while no difference between Si and Si with oxide can be observed. (b) FIBID Pt on Si with Cs^+ ions at 2 kV showing the highest amount of bubbles. (c) Pt deposited at 16 kV with no bubbles.

EDS measurements in Fig. 2 show that these bubbles are mainly consisting of Cs and oxygen (O). The theory proposed in Ref. [10] can therefore also explain the surface bubbles on Cs^+ FIBID-Pt. The proposed forming mechanism for these bubbles is that volatile elements in the Pt precursor trap the primary alkali metal ions when the chemical bonds of the precursor are not completely broken. When low-energy ions induce deposition, a smaller amount of SE is produced that can break precursor bonds compared to deposition with high-energy ions, leading to leftover volatile elements. This is why only 2 and 5 kV Cs^+ deposition lead to surface bubbles. With higher ion exposure, the volatile elements are sputtered away; therefore, the surface bubbles diminish with higher ion doses.

Because the Pt layers deposited with Cs^+ ions at 2 kV are so sensitive to air exposure, the deposition rate and the resistivity measurements will mainly focus on acceleration voltages of 5, 8, and 16 kV.

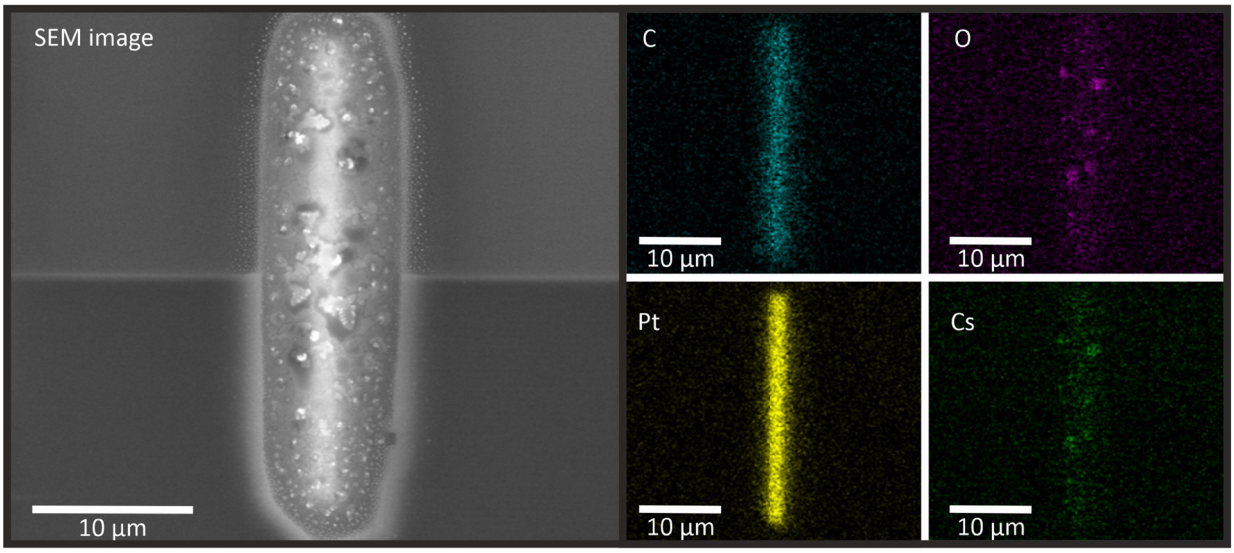

Figure 2: SEM and EDS analysis of Pt layer deposited at 2 kV with Cs^+ ions. The SEM image shows an overview of the layer, while the other images depict the individual material distribution. The actual shape of the layer can be seen in the images of the Pt and C concentration, while the bubbles mainly consist of Cs and O. While the highest concentration of Pt and C can be found within the actual shape, the Cs and O distribution correspond to the bubble area in the SEM image.

Deposition rates

Deposition rates of Ga^+ and Cs^+ FIBID-Pt (displayed in Fig. 3) were measured with the cross section dimensions determined via FIB cut and SEM imaging. The deposition rates of Pt on Si increase with increasing ion current density. This applies to almost all voltages for Cs^+ as well as Ga^+ ions. Only for Ga at 30 kV and a current density > 6 pA/μm^2 the growth rate is lower compared to all other beam parameters. This is due to the fact that the sputter rate increases with beam current while the deposition rate is saturated by the limited gas flow, which leads to an overall lower increase in the growth rate with increasing current density. This agrees with previous findings for Ga^+ FIBID-Pt [23]. Also, for Cs^+ at 5 kV, the deposition rate is lower. A possible explanation might be the broader beam diameter, which increases with lower acceleration voltages (< 5 kV) and higher ion beam currents (> 200 pA). This leads to a lower current density in each beam spot compared to higher voltages with the same ion beam current. Thus, while the overall current density (ion beam current per pattern size) is the same, the local density is lower which results in

a lower growth rate. In the future, further measurements could be done with finer variations of the ion beam current starting at 100 pA and 5 kV to verify this assumption.

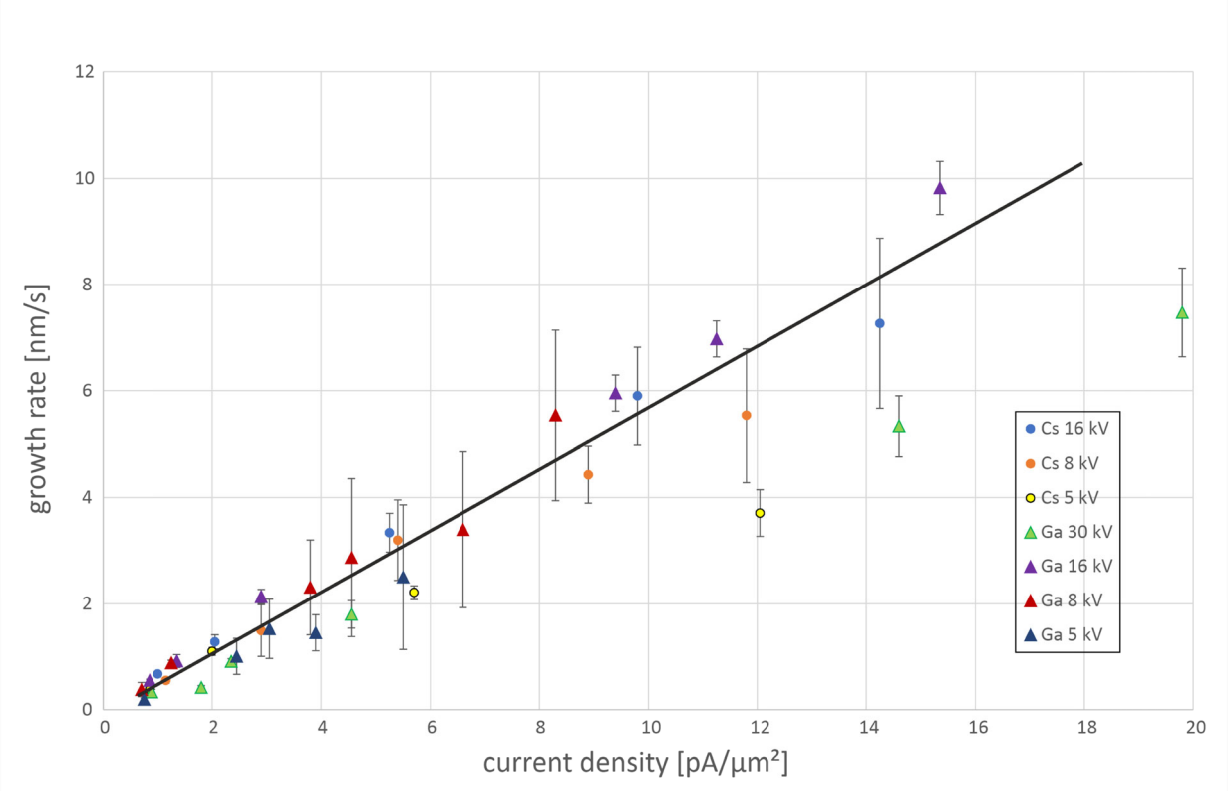

Figure 3: Pt growth rate vs. ion current density for different acceleration voltages of Cs^+ and Ga^+ ions. As a "guide to the eye," a line for the average growth rate is shown. With increasing current density the growth rate increases. Only for Ga^+ ions at 30 kV and Cs^+ ions at 5 kV, the growth rate at higher current densities is much lower than the average.

Composition and microstructure

Compositional data of the Cs^+ FIBID-Pt were calculated from the data provided by TEM-EDS analyses. An exemplary acquired EDS map for the 16 kV 54 pA Cs^+ FIBID-Pt is shown in Fig. 4. The Si-rich region shown as the red area in the upper-right corner of the Si map corresponds to the Si substrate. Before the TEM sample preparation process, a C layer of focused electron beam induced deposition (FEBID) was coated on top of the Cs^+ FIBID-Pt deposits. Therefore, a C-rich region exists in the lower-left corner of the C map. EDS spectra were taken at five points within

the bulk deposit and then averaged to determine the chemical composition. Figure 5 displays these compositional data for C, O, Pt, and Cs with standard deviations of the average as uncertainties.

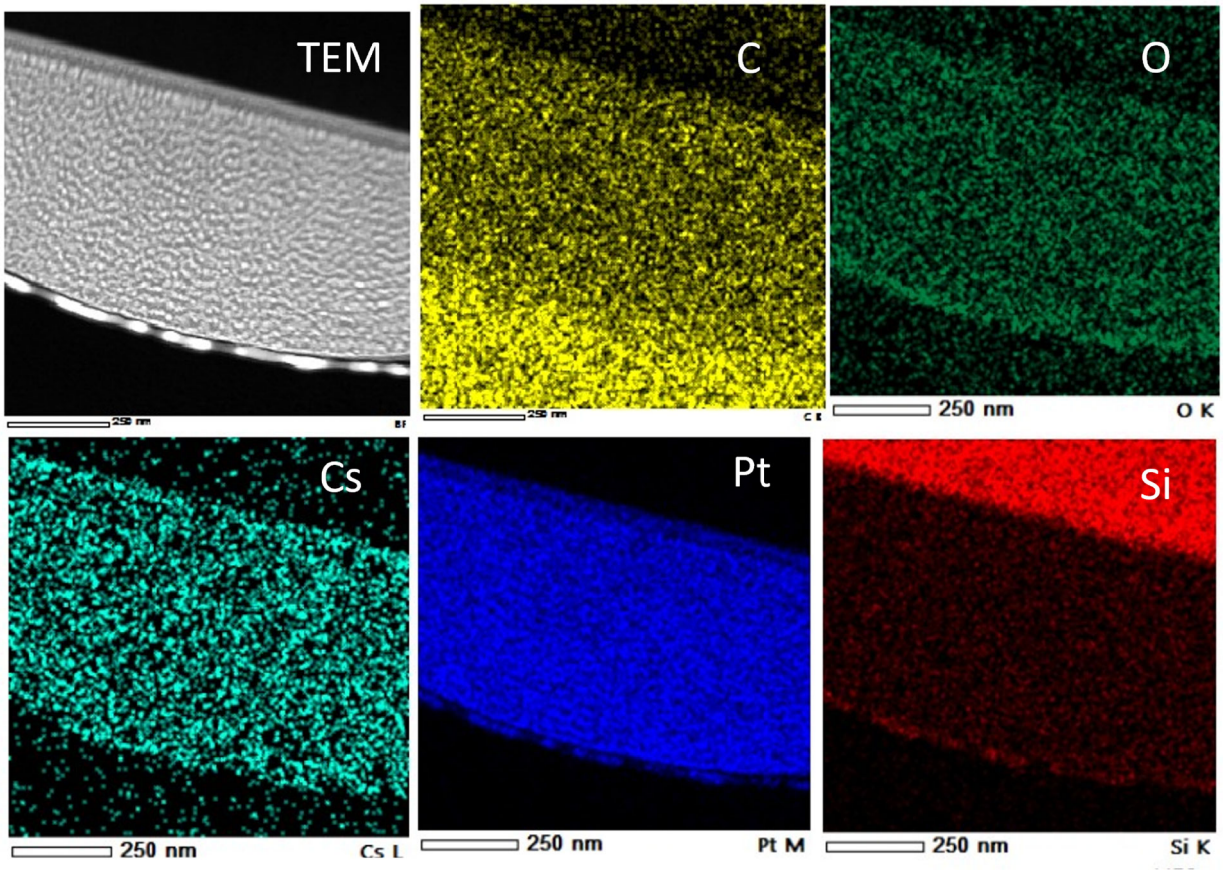

Figure 4: TEM-EDS mapping for Pt deposit induced by 16 kV 54 pA Cs^+

From the data shown in Figure 5 it follows that the Pt deposits created at 8 kV and 10 pA Cs^+ result in an atomic ratio of C:O:Pt:Cs = 74:2.5:23:1. Compared to Rb^+ FIBID-Pt of similar beam energy, current, and ion dose (8.5 kV 10 pA Rb^+ delivers C:O:Pt:Rb = 25:20:49:5) presented in Ref. [10], Cs^+ FIBID-Pt has lower O, Pt, and Cs contents and higher C content. This C content could be partially affected by the FEBID-C protective layer for the TEM sample. However, the EDS data were reported without adjustment to the C% data because the 2 kV 54 pA Cs^+ FIBID-Pt included in Fig. 5 exhibits much lower C% despite being on the same TEM lamella as the other deposits. In addition, very little Si% appears within the deposit area, which demonstrates the location sensitivity of TEM-EDS. This location sensitivity should help to show that the FEBID-C protective layer is

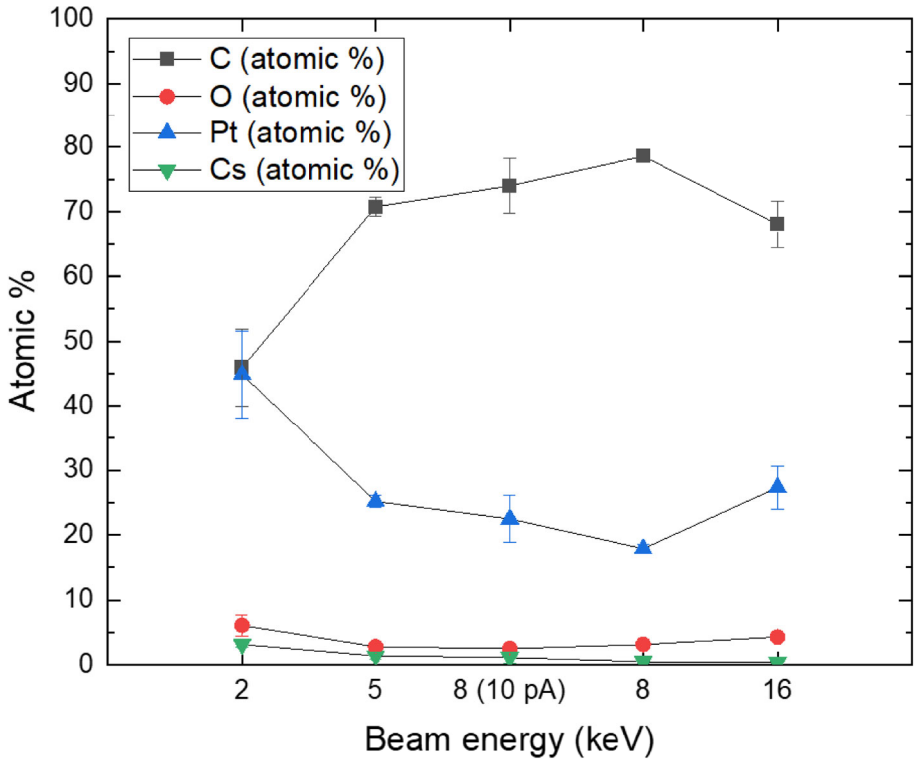

Figure 5: Cs^+ induced Pt composition data. Other than for the 8 kV 10 pA data, 54 pA was used for deposition with different beam energies

not the main contributor to the higher C% of Cs^+ FIBID-Pt. The composition of the Cs^+ FIBID-Pt stays mostly constant for beam energies above 2 kV. The 2 kV Cs^+ FIBID, being closer to Rb^+ FIBID-Pt in Pt% and C%, is an outlier compared to the FIBID under higher beam energies. The cause for the higher C% in Cs^+ FIBID-Pt however remains unclear to the authors at this stage.

As with Rb^+ and Ga^+, Cs^+ FIBID-Pt also contains crystalline Pt grains embedded in a C-rich matrix, as shown in Fig. 6. These bright field TEM images were used for grain diameter measurements in the same way as done in Ref. [10]. The average grain diameter grows from 1.9 nm to 5.8 nm when the beam energy increases from 2 kV to 16 kV. The increase in grain size with beam energy is visually obvious from the bright field images shown in Fig. 6. Previously, De Teresa et al. reported a 3.2 ± 0.8 nm grain diameter for 5 kV Ga^+ FIBID-Pt [23], which is similar to the 2.7 ± 0.3 nm grain diameter for 5 kV Cs^+ FIBID-Pt. The grain diameter of 5.8 nm at 16 kV Cs^+ FIBID-Pt is similar to those of 8.5 kV Rb^+ and 8 kV Ga^+ FIBID-Pt. Thus, lower energy Cs^+ creates deposits

with finer grains. It is worth noting that the growth in grain diameter does not correlate with the EDS data, in which the composition remains nearly constant for above 2 kV Cs^+ FIBID-Pt.

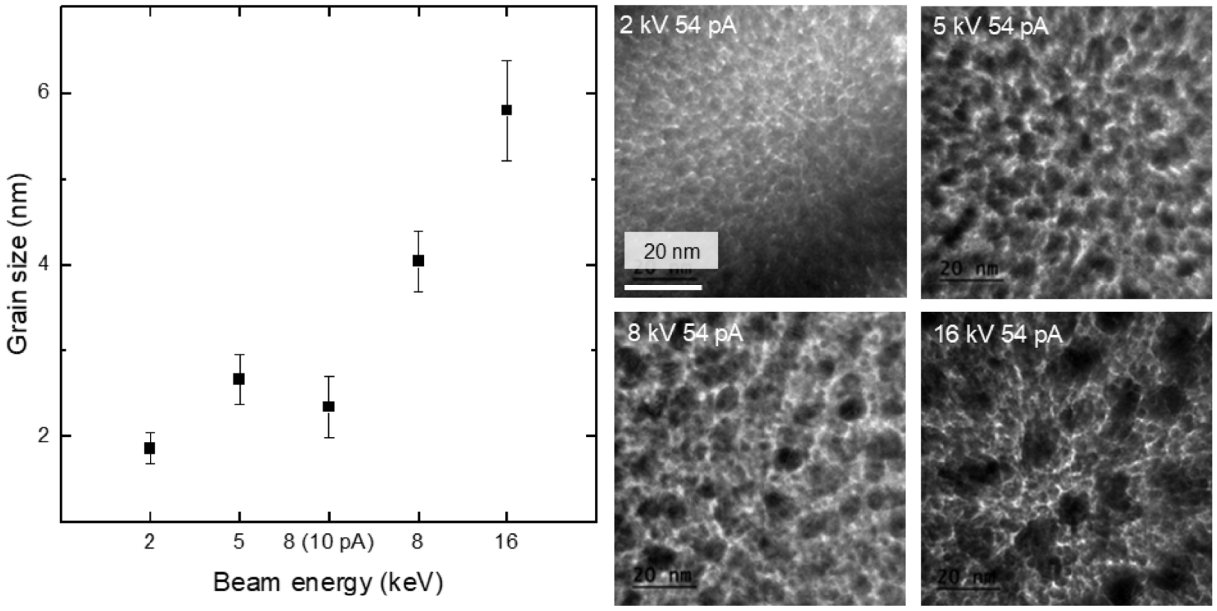

Figure 6: Bright field images of Cs^+ induced Pt deposit and Pt grain size data for different acceleration voltages

Deposit resistivity

The specific resistance was measured with a 4-probe-set-up as shown in Fig. 7(a). The electric current was pushed trough the deposited layer with the two upper contacts, while the voltage was measured between the two lower contacts to evaluate the resistance R in the same way as in Ref. [10]. After these measurements were done, the area A of the cross section was determined with a FIB cut and SEM image (see Fig. 7(b)). The length l between the contacts was about 14.6 µm so the specific resistance can be calculated with $R = \rho A/l$ for each layer.

For each beam setting, the deposition time was calculated with the growth rate shown in Fig. 3. Pt layers with a thickness of 1 µm should be deposited but, because here the substrate is glass and not Si, the estimated and real layer thickness differ. Overall they vary from 300 to 1200 nm. In theory the area of the cross section should not have an influence on the calculation of the specific resistivity, however, De Teresa et al. showed there is an impact [24] [25]. Therefore, preliminary measure-

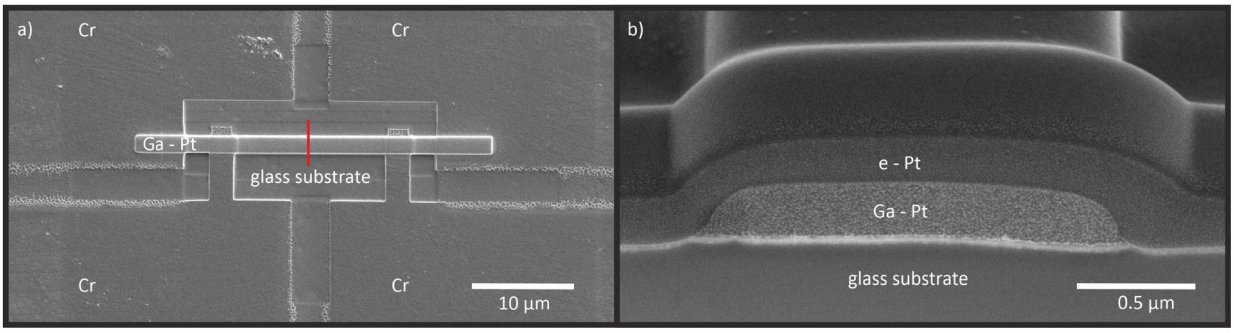

Figure 7: (a) structure for the resistivity measurements consisting of four Cr electrodes and the 35 µm by 1.5 µm Ga induced Pt deposit layer. The red line indicates the position of the cross section (b) SEM image of this cross section. Before the FIB cut for the cross section measurement was done, an additional Pt layer was deposited with FEBID for protection

ments were carried out. With the Ga^+ FIB, Pt layers were deposited with an ion current density of 6 pA/μm^2 at a voltage of 30 kV. Only the deposition time and thus the layer thickness was varied. The results can be seen in Figure 8 (a). Layers thicker than 1 µm have a lower specific resistance compared to the thinner once. The specific resistance can almost be halved. So for this setup, the layer thickness has an influence on Ga^+ FIBID-Pt.

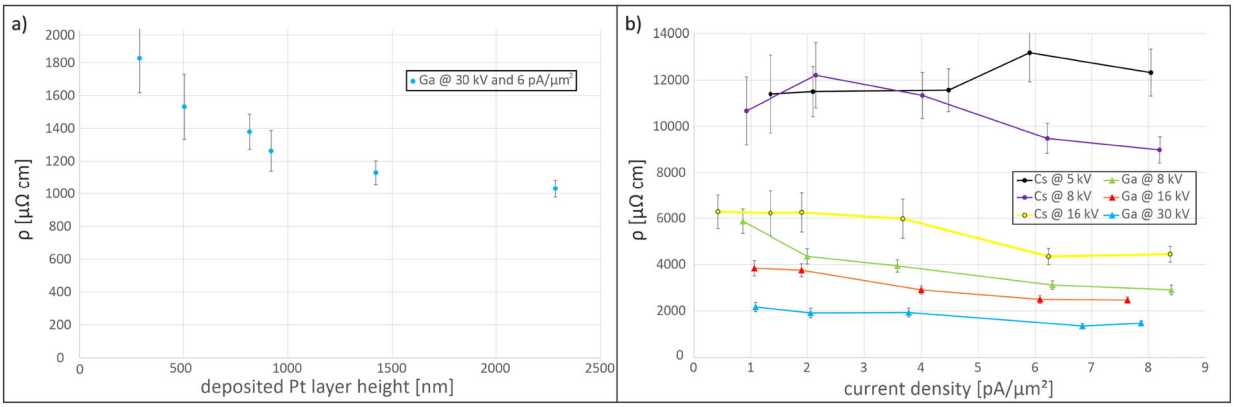

Figure 8: (a) Ga^+ induced Pt deposit for resistivity measurement at the same current density and acceleration voltage. Only the layer thickness was varied. Thicker layers have a lower specific resistance. (b) Specific resistance vs. current density for different acceleration voltages for Ga^+ and Cs^+ ions. With increasing acceleration voltage, the specific resistance decreases. Furthermore, the Ga^+ FIBID-Pt has a lower resistance than Cs^+ FIBID-Pt.

Figure 8 (b) contains the measured resistivity results for Ga^+ and Cs^+ ions for different current densities and acceleration voltages. The resistivity of Cs^+ FIBID-Pt decreases with increasing primary ion beam energy. For 16 and 8 kV Cs^+ FIBID-Pt, the resistivity also decreases with higher Cs^+ ion

current density. Only for 5 kV the resistance increases at higher beam currents. For all acceleration voltages using Ga^+ ions, i.e., 30, 16, and 8 kV, respectively, the specific resistance decreases with increasing current density. Overall the resistance of Cs^+ FIBID-Pt is at all voltages higher than Ga^+ FIBID-Pt. Only Pt deposited with Cs^+ ions at 16 kV has almost the same value of Ga^+ FIBID-Pt. The other voltages create layers with at least three times higher specific resistivity values.

The decrease in resistivity for Ga^+ FIBID-Pt with increasing ion current has already been reported [26] and is now verified in this measurements. Especially the Cs^+ FIBID-Pt layers with a current density < 6 pA/μm^2 have thicknesses < 1 µm. As shown in 8 (a), this may also lead to a higher specific resistance. The changes in resistivity are not immediately obvious from the chemical composition information of the deposits. Speculation based on the microstructure provides a probable cause for this decreasing resistivity versus beam energy. The average diameter of Pt-rich grain grows for FIBID under higher beam energy. With larger grain diameters, the Pt-rich particles have larger surface areas in close contact. This large surface area helps the current to flow more easily within the Pt deposit. Therefore, the deposit resistivity decreases despite a similar chemical composition. However, it is unclear why Cs^+ FIBID-Pt would have a higher resistivity than Ga^+ FIBID-Pt under similar beam conditions since the Cs^+ FIBID has the lowest O%, which should lead to a smaller resistivity. So it might be a combined chemical composition and grain size effect. So far, the acceleration voltage and the ion species seem to have a more dominant role than the current density for the specific resistance. Further studies are required to fully investigate the resistivity-microstructure dependency for FIBID-Pt.

To compare the Cs^+ and Rb^+ FIBID, Pt layers were deposited with the same beam settings: a very low current density of about 0.2 pA/μm^2 at a voltage of 8 kV. The specific resistance of Cs^+ FIBID-Pt is $(3.2 \pm 0.4) \times 10^4$ $\mu\Omega$ cm, which is about 25 percent lower compared to Rb^+ FIBID-Pt with a resistance of about $(12 \pm 4) \times 10^4 \mu\Omega$ cm [10]. Also, one Pt layer was deposited with Cs^+ ions at 2 kV and a beam current density of 3.76 pA/μm^2. Here the resistance is $(3.4 \pm 0.3) \times 10^4$ $\mu\Omega$ cm which is three to five times higher compared to other Cs^+ induced Pt layers. So, alkali-metal

ion sources operating with low current densities and acceleration voltages evoke high specific resistance.

Conclusion

In this paper we show that it is possible to deposit Pt with a Cs^+ FIB. The growth rate was measured for Ga^+ and Cs^+ ions at different acceleration voltages. The rate increases mainly linearly with ion current density. Pt layers deposited with Cs^+ ions at 2 and 5 kV react with air and form bubbles. This similarity in surface bubbles between Cs^+ and Rb^+ may reveal a characteristic phenomenon of alkali metal ion-induced deposition. The specific resistance of the deposited Pt decreases with increasing acceleration voltage and is mostly independent of the ion current density. The Cs^+ FIBID-Pt, with a lower Pt content, has resistivity values between those of Ga^+ and Rb^+ FIBID-Pt. Lower current densities and acceleration voltages were found to evoke a higher specific resistance.

Funding

This work is part of the project Next-Generation Focused Ion Beam (NWO-TTW16178) of the research program Applied and Engineering Sciences (TTW), which is (partly) financed by the Dutch Research Council (NWO). The authors are all members of the FIT4NANO COST Action CA19140.

References

1. Alkemade, P. F. A.; Miro, H. *Appl. Phys. A* **2014**, *117*, 1727–1747.

2. Utke, I.; Hoffmann, P.; Melngailis, J. *J. Vac. Sci. Technol. B* **2008**, *26*, 1197.

3. Gazzadi, G.; Mulders, J.; Trompenaars, P.; Ghirri, A.; Rota, A.; Affronte, M.; Frabboni, S. *Microelectronic Engineering* **2011**, *88*, 1955–1958.

4. Orús, P.; Sigloch, F.; Sangiao, S.; Teresa, J. M. D. *Nanomaterials* **2022**, *12*, 1367.

5. Höflich, K.; Hobler, G.; Allen, F. I.; Wirtz, T.; Rius, G.; McElwee-White, L.; Krasheninnikov, A. V.; Schmidt, M.; Utke, I.; Klingner, N.; Osenberg, M.; Córdoba, R.; Djurabekova, F.; Manke, I.; Moll, P.; Manoccio, M.; Teresa, J. M. D.; Bischoff, L.; Michler, J.; Castro, O. D.; Delobbe, A.; Dunne, P.; Dobrovolskiy, O. V.; Frese, N.; Gölzhäuser, A.; Mazarov, P.; Koelle, D.; Möller, W.; Pérez-Murano, F.; Philipp, P.; Vollnhals, F.; Hlawacek, G. *Appl. Phys. Rev.* **2023**, *10*, 041311.

6. Utke, I.; Michler, J.; Winkler, R.; Plank, H. *Micromachines* **2020**, *11*, 397.

7. Chen, P.; Salemink, H. W. M.; Alkemade, P. F. A. *J. Vac. Sci. Technol. B* **2009**, *27*, 2718.

8. McClelland, J. J.; Steele, A. V.; Knuffman, B.; Twedt, K. A.; Schwarzkopf, A.; Wilson, T. M. *Appl. Phys. Rev.* **2016**, *3*, 011302.

9. Xu, S.; Li, Y.; Vredenbregt, E. J. D. *J. Vac. Sci. Technol. B* **2022**, *40*, 042801.

10. Li, Y.; Xu, S.; Sezen, M.; Misirlioglu, F. B.; Vredenbregt, E. J. D. *J. Vac. Sci. Technol. B* **2023**, *41*, 042803.

11. Li, Y. Characterization and Application of an Ultracold Rubidium Focused Ion Beam. Ph. D. Thesis, Eindhoven University of Technology, 2023. available at https://research.tue.nl/files/313563364/20231215_Li_Y._hf.pdf

12. Knuffman, B.; Steele, A. V.; McClelland, J. J. *J. Appl. Phys.* **2013**, *114*, 044303.

13. Steele, A. V.; Schwarzkopf, A.; McClelland, J. J.; Knuffman, B. *Nano Futures* **2017**, *1*, 015005.

14. zeroK Nanotech, Cs FIB: Zero. https://www.zerok.com/products.html#FIBZERO_GOTO (accessed Aug 01, 2023).

15. Li, Y.; Xu, S.; Loeber, T. H.; Vredenbregt, E. J. D. *Microscopy and Microanalysis* **2024**, *30*, 817–824.

16. Loeber, T. Benefits of a Cs FIB with a low temperature ion source compared to a standard Ga FIB. https://www.zerok.com/assets/slides/Krakau2022.pdf (accessed Oct 01, 2023).

17. Storms, H. A.; Brown, K. F.; Stein, J. D. *Anal. Chem.* **1977**, *49*, 2023–2030.

18. Castro, O. D.; Audinot, J.-N.; Hoang, H. Q.; Coulbary, C.; Bouton, O.; Barrahma, R.; Ost, A.; Stoffels, C.; Jiao, C.; Dutka, M.; Geryk, M.; ; Wirtz, T. *Anal. Chem.* **2022**, *94*, 10754–10763.

19. Wirtz, T.; Migeon, H.-N. *Surface Science* **2004**, *557*, 57–72.

20. Priebe, A.; Michler, J. *Ultramicroscopy* **2019**, *196*, 10–17.

21. Okumura1, T.; Tamura, K.; Fujii, E.; Yamada, H.; Kogure, T. *Microscopy* **2014**, *63*, 65–72.

22. Yoshigoe, A.; Shiwaku, H.; Kobayashi, T.; Shimoyama, I.; Matsumura, D.; Tsuji, T.; Nishihata, Y.; Kogure, T.; Ohkochi, T.; Yasui, A.; Yaita, T. *Appl. Phys. Lett.* **2018**, *112*, 021603.

23. Teresa, J. M. D.; Córdoba, R.; Fernández-Pacheco, A.; Montero, O.; Strichovanec, P.; Ibarra, M. R. *J. Nanomater.* **2009**, *2009*, 936863.

24. Teresa, J. M. D.; Cordoba, R.; Fernandez-Pacheco, A.; O.Montero,; Strichovanec, P.; Ibarra, M. R. *Journal of Nanomaterials* **2009**, 936863.

25. Fernández-Pacheco, A.; Teresa, M. D.; Córdoba, R.; Ibarra, M. R. *PHYSICAL REVIEW B* **2009**, *79*, 174204.

26. Telari, K. A.; Rogers, B. R.; Fang, H.; Shen, L.; Weller, R. A.; Braski, D. N. *J. Vac. Sci. Technol. B* **2002**, *20*, 590.